Single-atom Co embedded in BCN matrix to achieve 100% conversion of peroxymonosulfate into singlet oxygen

Xue Zhao [a,b,1], Xue Li [a,1], Zhu Zhu [a], Wanbiao Hu [a], Haibo Zhang [b], Jian Xu [c], Xun Hu [d], Yingtang Zhou [e,*], Ming Xu [f,*], Hucai Zhang [a], Guangzhi Hu [a,*]

[a] Institute for Ecological Research and Pollution Control of Plateau Lakes, School of Ecology and Environmental Science, Yunnan University, Kunming 650504, China
[b] College of Chemistry and Molecular Sciences, Wuhan University, Wuhan 430072, China
[c] State Key Laboratory of Environmental Criteria and Risk Assessment, Chinese Research Academy of Environmental Sciences, Beijing 100012, China
[d] School of Material Science and Engineering, University of Jinan, Jinan 250022, China
[e] National Engineering Research Center for Marine Aquaculture, Marine Science and Technology College, Zhejiang Ocean University, Zhoushan 316004, China
[f] State Key Laboratory of Chemical Resource Engineering, Beijing Advanced Innovation Center for Soft Matter Science and Engineering, Beijing University of Chemical Technology, Beijing 100029, China

ARTICLE INFO

ABSTRACT

Effective removal of pollutants that affect human health and ecosystem stability is a crucial challenge. Here, the structural confinement engineering strategy realizes the effective anchoring of atomically dispersed Co in the B-doped-CN network (BCN) (BCN/CoN[2 +2]). The advanced oxidation process (AOP) involved BCN/CoN[2 + 2] has realized the rapid and complete degradation to tetracycline (TCL), the removal of approximately 80% and 100% of tetracycline was achieved in 5 min and 30 min, respectively. The AOP with BCN/CoN[2 + 2] can degrade TCL over a wide pH; in addition, BCN/CoN[2 + 2] has the ability to efficiently degrade common pollutants, and its catalytic activity did not decay even if it was used repeated five times. Electron paramagnetic resonance (EPR) spectroscopy shows that BCN/CoN[2 + 2] drives the complete conversion of peroxymonosulfate (PMS) to $^1O_2$, and density functional theory calculations demonstrate that the base for the conversion of PMS to $^1O_2$ is from the isolated state of the active site Co.

1. Introduction

The rapid development of industrial, agricultural, and pharmaceutical fields has resulted in an increase in the number of pollutants that are discharged into the environment (water system and soil), thereby posing a danger to human health [1–4]. Compared with harmful heavy metals, organic pollutants pose high toxicity, wide-spreading range, strong persistence, and refractory degradation, which have a more serious impact on the ecological environment [5]. These harmful pollutants are conventional treated via physical adsorption, chemical adsorption, and biodegradation [6]. However, treating the pollutants in water and soil environments is challenging owing to inefficient treatment methods. For instance, adsorption pathways (especially chemical adsorption) sometimes result in secondary pollution and produce a large amount of solid waste; in addition, the desorption of pollutants requires a large amount of capital investment [7]. Biological purification is limited by slow kinetics; therefore, treating large sewage systems is challenging [8]. Remarkably, the advanced oxidation process (AOP) method developed in recent years involving the participation of peroxymonosulfate (PMS) has shown strong environmental remediation capabilities, and thus, it has attracted significant attention [9]. Particularly, sulfate radicals ($SO_4^{\cdot-}$), hydroxyl radicals (·OH), and singlet oxygen ($^1O_2$) produced by PMS can mineralize the organic pollutants such as organic dyes, pharmaceutical antibiotics, organic pesticides, organic surfactants, and most industrial fine chemicals into non-toxic and harmless CO_2 and H_2O [10,11].

The bond energies of O–O bond in PMS can reach 144 kJ mol^{-1}, which implies that PMS needs to be driven by an external force to be activated [12]. Generally, PMS can be converted into reactive oxygen species (ROS) with oxidizing ability under light, thermal, ultrasonic, or transition metal drives [13–17]. Obviously, the generation of light, heat, and ultrasound requires a large amount of energy input that relies on

complex equipment; however, transition metal catalysts can spontaneously activate PMS without any external energy input. Originally, homogeneous cobalt was widely used as a catalyst to activate PMS, because Co^{2+} and Co^{3+} have good valence changes ($Co^{2+} + HSO_5^- \rightarrow Co^{3+} + SO_4^{\cdot-} + OH^-$ and $Co^{3+} + HSO_5^- \rightarrow Co^{2+} + SO_5^{\cdot-} + H^+$) [18,19]. Although this is an effective method in driving PMS to generate ROS with high efficiency and low energy consumption, the homogeneous system faces the problem of difficulty in catalyst recovery and secondary pollution of metal ions [20,21]. As an improvement, carbon materials and metal oxides as supports have realized the transformation of cobalt-based catalysts from homogeneous to heterogeneous [22,23]. While the restriction of the carrier stabilizes the catalytic-active site, it also changes the reaction pathway of PMS activation with the participation of cobalt. In the studies performed with N-coordinated cobalt-based materials (Co-N-C) as catalysts, the conversion pathways of PMS are not uniform, which leads to differences in the types of ROS. Generally, $SO_4^{\cdot-}$ and $\cdot OH$ are produced through free radical pathways, whereas $^1O_2$ is produced through non-radical pathways [24,25]. However, the present challenge lies in the understanding of the mechanism of action in the AOP, and the focus is on the type of ROS that plays a key role in the process of pollutant degradation. This is because the conversion of PMS usually involves both free radical and non-free radical pathways, which is not conducive to the clarity of the degradation process [24,26–29]. In this context, Mi et al. performed the conversion of PMS into specific ROS with high selectivity after anchoring single-atom Co on an N-doped C-based material [30]. Due to the uniqueness of ROS species, the degradation mechanism of AOP under the participation of PMS is more clear, which is conducive to the development of advanced catalysts with structure-controlled for AOP.

Here, we developed a new strategy to achieve the structural control of cobalt-based materials, where the metal boron cluster organic polymer with phenanthroline complexing Co as the precursor was further annealed to prepare an AOP single-atom catalyst (BCN/CoN[2+2]) with B-doped and N split coordination Co. AOP driven by BCN/CoN[2+2] shows the characteristics of rapid degradation reaction kinetics and complete removal of tetracycline pollutants, wherein approximately 80% and 100% of TCL (50 mg L^{-1}) was removed in only 5 and 30 min, respectively. In addition to the ability to easily remove TCL from acidic or alkaline environments, AOP with BCN/CoN[2+2] has also demonstrated the ability to efficiently degrade various pollutants, even for chloramphenicol, which is difficult to degrade, achieving close to 80% degradation ratio. In addition, BCN/CoN[2+2] exhibits excellent cycle stability, even if it is recycled five times, and its catalytic activity maintains its initial level, which is important for further industrial applications. The process of 100% conversion of PMS into singlet oxygen by the Co single-atom site obtained by the mechanism of structural confinement (coordination anchoring) creates a unique degradation path of TCL, which provides an important reference for the mechanism of AOP involving different ROS.

2. Experimental section

2.1. Chemicals

Cesium-*closo*-dodecaborate ($Cs_2[B_{12}H_{12}]$, 98%) was prepared by referring according to a previously reported method [31–33]. *Caution! The preparation process of $Cs_2[B_{12}H_{12}]$ will produce a large amount of H_2* [34], *so ensure that the operating environment is free of fire and well ventilated.* Other reagents (analytical grade) were purchased from Aladdin Chemical Reagent Co., Ltd., and used as is. Milli-Q ultrapure water (18 MΩ cm^{-1}) was used throughout the experiment.

2.2. Material preparation

2.2.1. Synthesis of MBOPs

Herein, 1,10-phenanthroline of 1.190 g was dissolved in 300 mL of water at 90 °C, and subsequently, 0.223 g of $Zn(NO_3)_2.6H_2O$ and 0.437 g of $Co(NO_3)_2.6H_2O$ which were dissolved in 50 mL of water, was added to the 1,10-phenanthroline solution. After the resultant clear solution was aged for 30 min, 0.916 g of $Cs_2[B_{12}H_{12}]$ dissolved in 100 mL of water was added to the aged solution, following which a yellow suspension was obtained. After stirring the resultant solution for 1 h, the precipitate was filtered, and the obtained filter cake was washed alternately with water and ethanol three times and then dried in vacuum at 90 °C for 6 h. The obtained metal boron cluster organic polymer precursors are referred to as MBOPs.

2.2.2. Synthesis of MBOPs-1

1,10-phenanthroline of 1.190 g was dissolved in 300 mL of water at 90 °C, and then, 0.446 g of $Zn(NO_3)_2.6H_2O$ and 0.291 g of $Co(NO_3)_2.6H_2O$, which were dissolved in 50 mL of water was added to the solution. After the resultant clear solution was aged for 30 min, 1.102 g of $Cs_2[B_{12}H_{12}]$ which was dissolved in 100 mL of water and was added to it, and a yellow suspension was immediately obtained. After stirring the solution for 1 h, the precipitate was filtered, and the obtained filter cake was washed alternately with water and ethanol three times and subsequently dried in vacuum at 90 °C for 6 h. The obtained metal boron cluster organic polymer precursors were referred to as MBOPs-1.

2.2.3. Synthesis of MBOPs-2

Initially, 1.190 g of 1,10-phenanthroline was dissolved in 300 mL of water at 90 °C, and then 0.669 g of $Zn(NO_3)_2.6H_2O$ and 0.146 g of $Co(NO_3)_2.6H_2O$ were dissolved in 50 mL of water and added to the dissolved 1,10-phenanthroline. After the formed clear solution was aged for 30 min, 1.119 g of $Cs_2[B_{12}H_{12}]$ dissolved in 100 mL of water, was added and a yellow suspension was immediately formed. Following the stirring of the solution for 1 h, the precipitate was filtered, and a filter cake was obtained. The filter cake was washed alternately with water and ethanol three times and then dried in vacuum at 90 °C for 6 h. The obtained metal boron cluster organic polymer precursors were referred to as MBOPs-2.

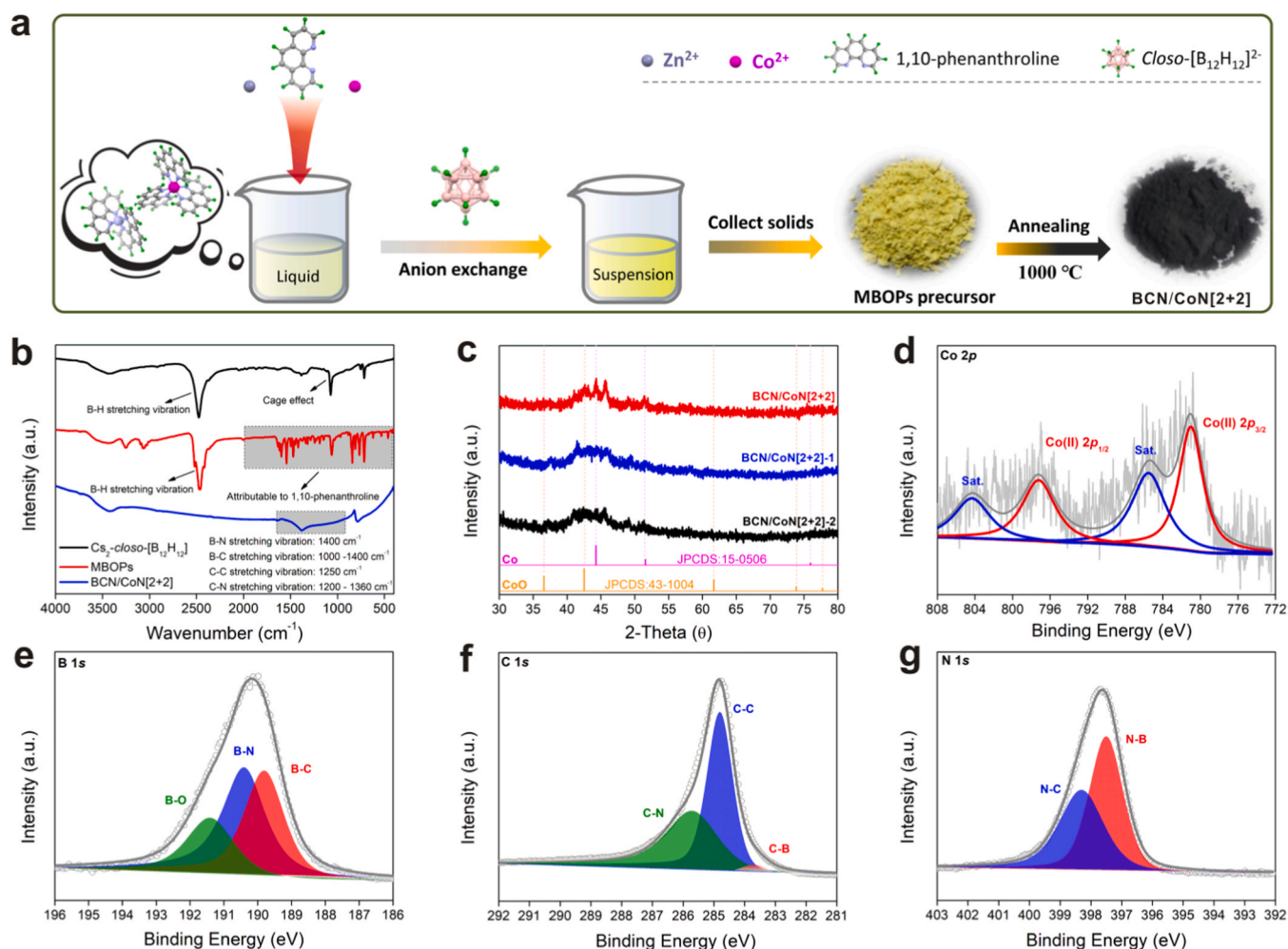#### 2.2.4. Synthesis of BCN/CoN[2+2], BCN/CoN[2+2]−1, and BCN/CoN [2+2]−2

The synthesized MBOPs were annealed as per the following procedure: In Ar gas atmosphere, the temperature was increased from 25 °C to 1000 °C at a heating rate of 5 °C/min and keep for 2 h, after which the temperature was allowed to reduce naturally. Following the annealing of MBOPs, MBOPs-1, and MBOPs-2, BCN/CoN[2+2], BCN/CoN[2+2]−1, and BCN/CoN[2+2]−2 were obtained, respectively.

2.2.5. Synthesis of CN/CoN[2+2]

Initially 1.190 g of 1,10-phenanthroline was dissolved in 300 mL of water at 90 °C, and then 0.223 g of $Zn(NO_3)_2.6$ H_2O and 0.437 g of $Co(NO_3)_2.6$ H_2O, which were dissolved in 50 mL of water was added to the dissolved 1,10-phenanthroline. After the formed clear solution was aged for 30 min, the solvent was removed by distillation under reduced pressure and vacuum dried at 90 °C for 6 h. Finally, according to the annealing procedure in Section 2.2.4, the vacuum-dried solid was annealed to obtain CN/CoN[2+2] without B as a dopant.

2.3. Material characterization

Infrared spectroscopy (FTIR) was performed on a Fourier transform infrared spectrometer (Thermo iS10) to determine the composition of the materials. The materials were mixed in high-purity potassium bromide and pressed into flat for further analysis. Powder X-ray diffraction (PXRD) analysis of the materials was performed using an X-ray spectrometer (Bruker D8 Advance) equipped with a Cu target, and the signal scanning speed was 5 °/min. The X-ray photoelectron spectroscopy (XPS) of the material was performed using an X-ray photoelectron spectrometer (ESCALAB250Xi) to analyze the valence state distribution

Fig. 1. a) Schematic diagram of the preparation route of BCN/CoN[2+2]; **b**) FT-IR spectroscopy; **c**) PXRD pattern; **d**) XPS results (cobalt binding energy region) of BCN/CoN[2+2]; **e**) XPS results (boron element binding energy region) of BCN/CoN[2+2]; **f**) XPS results (carbon element binding energy region) of BCN/CoN[2+2]; **g**) XPS results (nitrogen element binding energy region) of BCN/CoN[2+2].

of the elements. Scanning electron microscopy (SEM) images were collected using a field emission scanning electron microscope (Zeiss SIGMA) with In-Lens mode, operating at an acceleration voltage of 5 kV. Transmission electron microscopy (TEM) images were collected using an FEI Themis Z electron microscope (equipped with energy scattering X-ray spectrometer accessories), including high-resolution transmission electron microscopy (HR-TEM) images and high-angle annular dark-field (HAADF) images. Electron paramagnetic resonance (EPR) spectra signals were recorded using a Bruker EMXPLUS instrument. The concentration of pollutants was examined using an ultraviolet-visible spectrophotometer (UV–vis, GENESYS 50). The Co K-edge XAS measurement was performed under the beam line 1W1B of the Synchrotron Radiation Facility (BSRF) in Beijing. Use the 4 f spectral peak of the newly sputtered gold wafer to calibrate the photon energy, and then normalize the spectrum to produce an edge jump of 1 [35].

2.4. Pollutant degradation program

Pollutants (50 mL) with accurate concentration were placed in a 250 mL Erlenmeyer flask, and then 30.0 mg of the catalyst was added. The Erlenmeyer flask was placed on a constant temperature shaker (temperature = 25 °C, shaking speed = 120 rpm). Finally, 30.0 mg of PMS was added and the reaction was noted. During the degradation period, the concentration of the pollutants was monitored using an ultraviolet-visible spectrophotometer. The absorbance wavelengths of tetracycline,

chloramphenicol, methyl orange, rhodamine, and p-nitrophenol solutions were 355, 270, 465, 554, and 300 nm, respectively. Accurate concentrations of all pollutants were obtained by standard curve interpolation (the tetracycline standard curve is shown in Fig. S1).
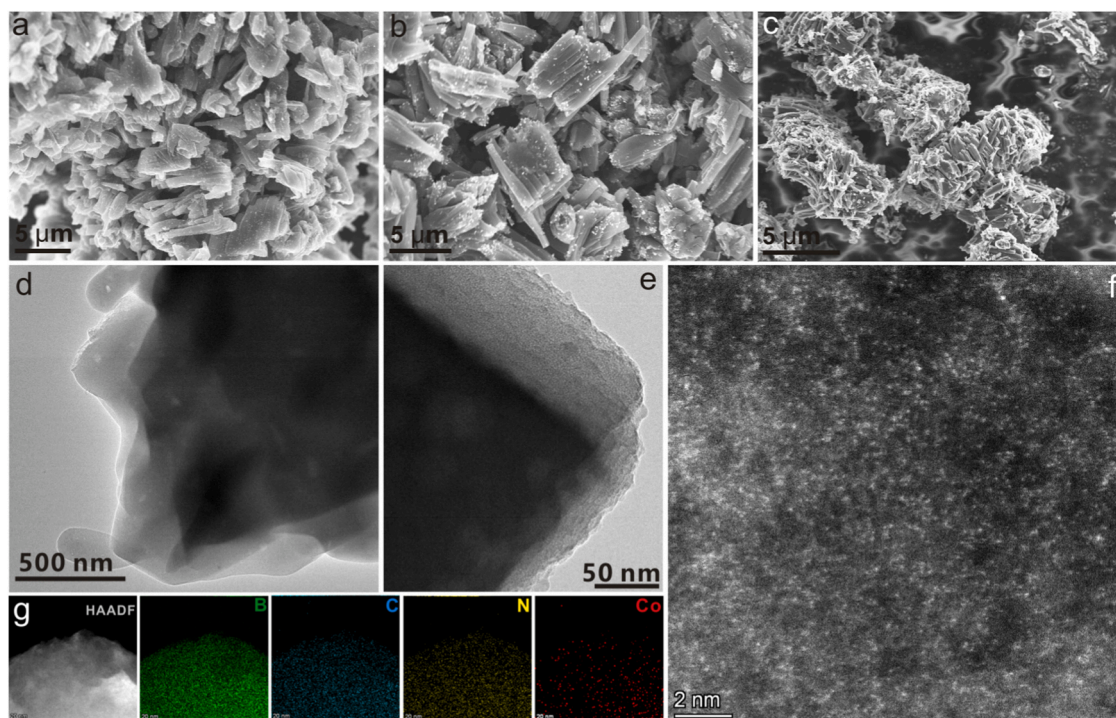
In the cycle experiment, after the degradation experiment, the catalyst was collected by filtration and washed with ultrapure water five times to completely clean the remaining organic matter and inorganic salt. Then the catalyst was directly used in the next round of cycling without drying. The initial value of the catalyst input in the cycle experiment is 30 mg, and no additional catalyst will be added when it was recycled and used in the next round of experiment.

3. Results and discussion

3.1. Catalyst preparation strategy and characterization

In this study, we innovatively developed a Co single-atom material anchored on a BCN matrix, in which structural confinement engineering is the main design strategy. Initially, the metal ions are separated by the complexation of the 1,10-phenanthroline rigid ligands and metal ions (Zn^{2+}, Co^{2+}). Then, large-sized $closo$-$[B_{12}H_{12}]^{2-}$ was introduced as a counter anion to quickly replace NO_3^- to separate the 1,10-phenanthroline metal complex clusters resulting in MBOPs. Finally, MBOPs were converted to BCN/CoN[2+2] via pyrolysis at 1000 °C (Fig. 1**a**). However, MBOPs have poor conductivity, and the formation of a BCN matrix

Fig. 2. a) SEM image of BCN/CoN[2+2]; **b)** SEM image of BCN/CoN[2+2]−1; **c)** SEM image of BCN/CoN[2 + 2]; **d-e)** TEM images of BCN/CoN[2+2]; **f)** TEM image (HAADF mode) of BCN/CoN[2 + 2]; **g)** Distribution mapping of B, C, N and Co in BCN/CoN[2+2].
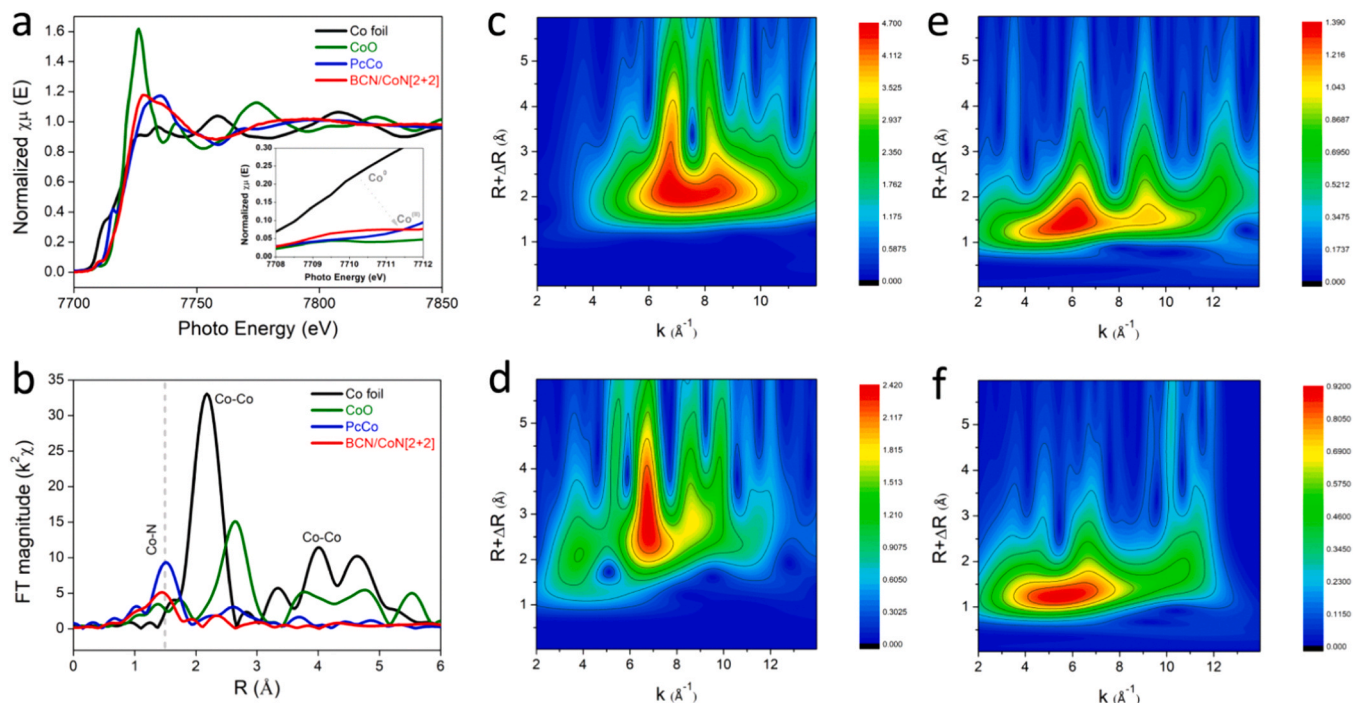
following pyrolysis can increase the electron transfer rate of the carrier. In addition, the more rigid BCN matrix is more mechanically stable than MBOPs. 1,10-phenanthroline was chosen as the organic ligand because it has a chelating site (pyridine-N) and the structure is not easily distorted, which can prevent metal atoms from contacting each other. However, it is not enough to form (1,10-phenanthroline-Co)(NO$_3$)$_2$, because the (1,10-phenanthroline-Co)$^{2+}$ group is still in a free state, and the pyrolysis process is difficult to effectively prevent encounter between metal atoms. After *closo*-[B$_{12}$H$_{12}$]$^{2-}$ was introduced, NO$_3^-$ in (1,10-phenanthroline-Co)(NO$_3$)$_2$ was quickly replaced to form (1,10-phenanthroline-Co)(B$_{12}$H$_{12}$) with a larger precipitation coefficient (the detailed mechanism is shown in Fig. S2). *Closo*-[B$_{12}$H$_{12}$]$^{2-}$ has a large size and pyrolysis stability, so it can effectively isolate the (1,10-phenanthroline-Co)$^{2+}$ group in the early stage of pyrolysis, thereby promoting the existence of Co as single atom form. FT-IR spectrum (Fig. 1b) shows that the resonance peaks of *closo*-[B$_{12}$H$_{12}$]$^{2-}$ and 1,10-phenanthroline simultaneously appeared in MBOPs, indicating that *closo*-[B$_{12}$H$_{12}$]$^{2-}$ was successfully introduced into the 1,10-phenanthroline metal complex. After pyrolysis, the infrared resonance peaks of *closo*-[B$_{12}$H$_{12}$]$^{2-}$ and 1,10-phenanthroline are lost in BCN/CoN[2 + 2], and the infrared resonance peaks such as B–N, B–C, C–C and C–N appear instead. The introduction of Zn controls the content of metallic Co; in addition, the evaporation of Zn during the pyrolysis process at 1000 °C leads to an increase in the specific surface area of the material. In PXRD (Fig. 1c), diffraction peaks of Co or CoO are not observed in BCN/CoN[2+2], BCN/CoN[2 + 2], and BCN/CoN[2+2]. In the diffraction pattern, the broad peak in the range of 40–46° corresponds to the BN species (JCPDS: 15–0576). It is challenging to confirm the existence of cobalt species from the diffraction pattern, because cobalt exists as single atoms or as amorphous nanoparticles.

Further, the existence form of each element in BCN/CoN[2 + 2] was identified by XPS (Fig. 1d). The XPS signal peaks appearing in the binding energy region of cobalt are attributed to the contribution of Co$^{(II)}$, and the peaks of 780.8 eV and 797.6 eV correspond to Co$^{(II)}$2p$_{3/2}$ and Co$^{(II)}$2p$_{1/2}$ (the corresponding satellite peaks are at 785.3 eV and 804.1 eV respectively). In addition, the composition of B, C, and N

elements is analyzed via XPS. The signal appearing in the binding energy region of element B is formed by coupling the signal peaks of the B–O, B–N, and B–C bonds (Fig. 1e). The signal appearing in the binding energy region of element C is formed by coupling the signal peaks of the C–N, C–C (sp^2), and C–B bonds (Fig. 1f). The signal appearing in the binding energy region of element N can be formed by coupling the signal peaks of the N–C and N–B bonds (Fig. 1g).

Electron microscopy technology further presents the microscopic morphology of catalysts. Fig. 2a, b and c show the SEM images of BCN/CoN[2 + 2], BCN/CoN [2 + 2]− 1 and BCN/CoN[2+2]−2, respectively, and they all show the nanobulk formed by the nanorods closely attached. There was no significant change in the morphology of BCN/CoN[2 + 2] when the content of cobalt was varied. Taking BCN/CoN [2 + 2] as an example, the morphology of the TEM images (Fig. 2d) collected is consistent with the SEM image. It is worth noting that even with the highest cobalt content, there is still no metal nanoparticles formed in BCN/CoN[2 + 2] (Fig. 2d-e). When the scale in the TEM image is 2 nm, many high-contrast bright spots with an atomic-scale distribution were observed (Fig. 2f). Generally, the brightness of metals with large atomic numbers in the HAADF mode is brighter than that of the inorganic B, C, and N substrates. Since the pyrolysis of the sample at 1000 °C for 2 h is sufficient to evaporate the entire zinc content in the system, the high-contrast bright spot in HAADF mode can be attributed to the single-atom dispersed cobalt. Further element mapping proves this (Fig. 2g), the B, C, N, and Co signals are uniformly distributed throughout the district. The signal of Co is still displayed without the presence of nanoparticles, which once again proves that cobalt exists in the BCN matrix as single atom. The hysteresis loop (Fig. S3) of BCN/CoN[2+2], BCN/CoN[2+2]−1, and BCN/CoN[2+2]− 2 demonstrates insignificant magnetization, indicating that Co is atomic-dispersed and anchored on the carrier. This information also clarified the results of PXRD (Fig. 1c), there is no signal peak of cobalt because cobalt in the form of a single atom has no crystal face characteristics. In addition, N$_2$ adsorption/desorption test gave the BET surface area of BCN/CoN[2+2], BCN/CoN[2 +2]− 1 and BCN/CoN[2+2]− 2 as 1.93 m^2 g^{-1}, 19.91 m^2 g^{-1} and 25.07 m^2 g^{-1}, respectively (Fig. S4). The

Fig. 3. a) X-ray absorption near edge structure (XANES) signals of Co foil, CoO, PcCo and BCN/CoN[2 + 2]; **b)** Extended X-ray absorption fine structure (EXAFS) signals of Co foil, CoO, PcCo and BCN/CoN[2 + 2]; **c-f)** Two-dimensional color patch image obtained after EXAFS signal via wavelet transformation (c: Co foil; d: CoO; e: PcCo; f: BCN/CoN[2 +2]).
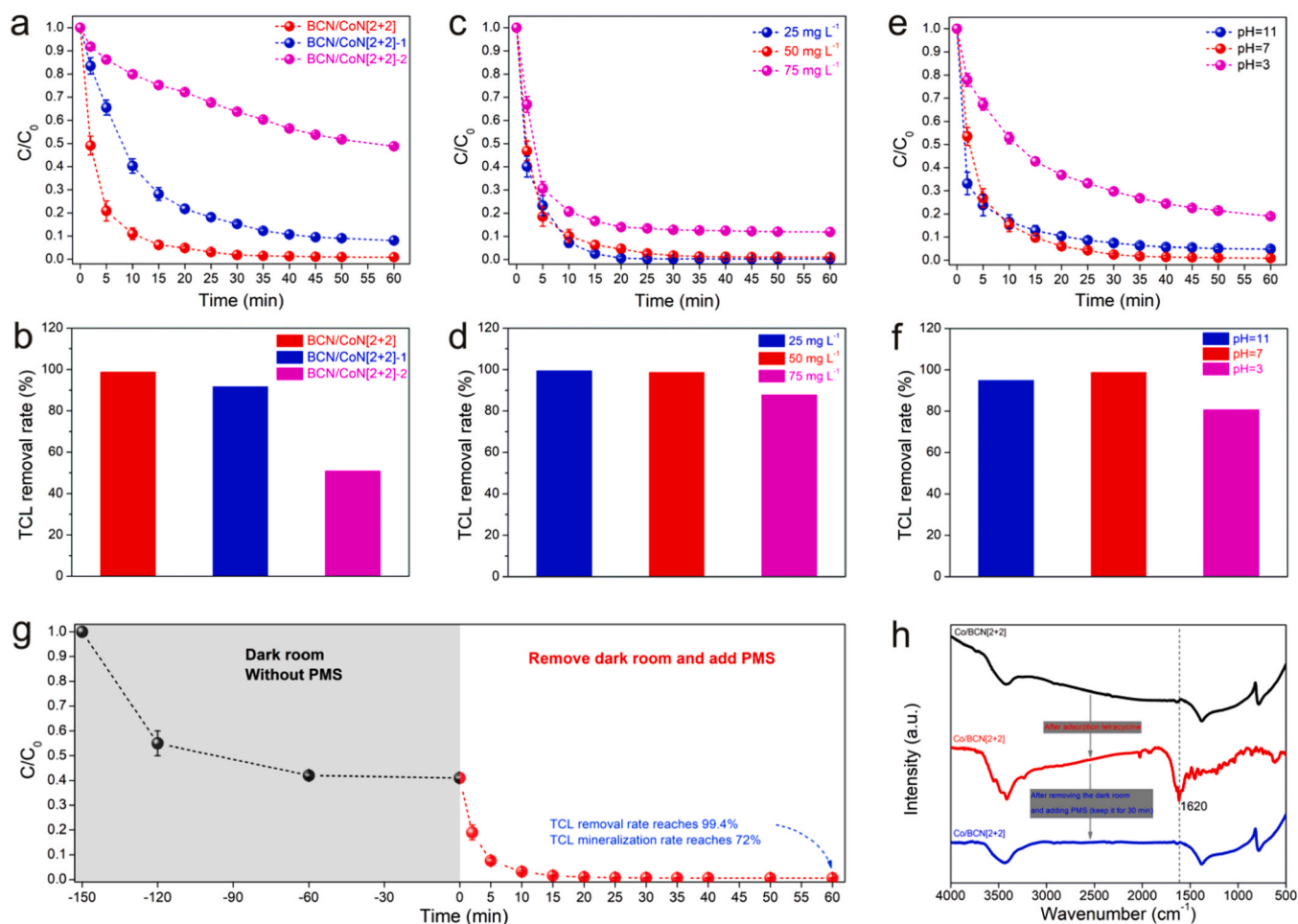
lower BET surface area value represents that BCN/CoN[2 + 2], BCN/CoN[2 + 2]− 1 and BCN/CoN[2 + 2]− 2 are not porous materials, which can also be inferred from their smooth nanorods morphology. Compared with BCN/CoN[2 + 2]− 2 and BCN/CoN[2 + 2]− 1, the BET surface area of BCN/CoN[2 + 2] is lower, because the former has a higher Co^{2+}/Zn^{2+} ratio. After annealing, the evaporation of Zn^{2+} can increase the pore density of the material, thereby obtaining a higher BET surface area.

Although XPS spectrum, PXRD spectrum, and TEM images have revealed some physicochemical characteristics of BCN/CoN[2+2], further characterization methods are still needed to reveal the coordination structure of Co in BCN/CoN[2+2]. The coordination environment and valence distribution of Co in BCN/CoN[2+2] are analyzed in detail based on the X-ray absorption near edge structure (XANES) and extended X-ray absorption fine structure (EXAFS) obtained from synchrotron. XANES shows that the signal of BCN/CoN[2 + 2] is very different from the signal of Co foil, but it is close to the signal of cobalt phthalocyanine (PcCo) (Fig. 3**a**). At lower photo energy, the valence of Co in BCN/CoN[2 + 2] is close to + 2 (inset in Fig. 3**a**) [36]. In EXAFS (Fig. 3**b**), BCN/CoN[2 + 2] and PcCo both show only one strong peak (at 1.5 Å), which is attributed to the contribution of the Co-N bond [37]. On the contrary, both Co foil and CoO showed Co-Co aggregate signals, the peaks at 2.2 Å and 4.1 Å were attributed to the signal of Co-Co bond [37]. In the two-dimensional color patch image obtained after EXAFS signal via wavelet transformation, a high-energy signal (red area) appears at 7.0 Å for Co foil (Fig. 3**c**) and CoO (Fig. 3**d**), which corresponds to the signal of the Co-Co coordination shell. The high-energy color patches of BCN/CoN[2 + 2] (Fig. 3**e**) and PcCo (Fig. 3**f**) are around 5.0 Å (in a single color block), which corresponds to the signal of the Co-N coordination shell. Based on this, it is proved that Co in BCN/CoN [2 + 2] exists in the form of + 2 valence (consistent with the results of XPS) and forms a Co-N coordination configuration. Note that in the signals after EXAFS and wavelet transformation, there is a slight offset between the BCN/CoN[2 + 2] signal and the PcCo signal. This is because Co in PcCo exists in the form of Co-N4, while the coordination configuration of Co in BCN/CoN[2 + 2] is attributed to the form of CoN

[2 + 2].

3.2. Pollutant degradation performance

As a potential catalyst, BCN/CoN[2 + 2] accelerates the rate of AOP. The effect of Co contents on the catalytic activity of BCN/CoN[2 + 2] was evaluated to determine the optimal structure and its active center. Under the same conditions, BCN/CoN[2 + 2] can greatly promote the degradation of TCL, and the catalytic activity of BCN/CoN[2+2]−1 is slightly lower (Fig. 4**a-b**). BCN/CoN[2+2]−2 has the least catalyst activity; its activity is approximately 50% of that of BCN/CoN[2 + 2]. In other words, BCN/CoN[2 + 2] with the highest Co content is most conducive to the degradation of TCL, which indicates that Co is the catalytically active center. Furthermore, TCL with concentrations of 25 mg L-1 and 50 mg L-1 can be almost completely degraded under the catalysis of BCN/CoN[2 + 2] (Fig. 4**c-d**). When the TCL concentration reached 75 mg L^{-1}, only approximately 88.5% TCL could be eliminated by BCN/CoN[2 + 2]. This is because the amount of ROS produced by a certain amount of PMS is fixed, and the degradation process stops as ROS is consumed. It should be noted that no matter the initial concentration of TCL is 25 mg L^{-1}, 50 mg L^{-1} or 75 mg L^{-1}, the degradation reaction within 0–5 min shows a consistent and similar trend of intensity. This result implies that PMS can be swiftly converted into ROS in the presence of BCN/CoN[2+2], and a high concentration of ROS promotes the degradation of TCL. The fatigue effect on the degradation of high concentrations of TCL appears only when the concentration of ROS is significantly reduced. In addition, the actual sewage environment is always related to the source of pollution, and thus, the pH of sewage is always in a state of change. Fig. 4**e-f** show the results of TCL degradation by BCN/CoN[2+2] in water systems with different pH values. Neutral and alkaline conditions marginally affect the catalytic activity of BCN/CoN[2+2]; however, the degradation process under acidic conditions is hindered to a certain extent. When pH = 3, the degradation rate is significantly lower than the neutral and alkaline conditions from the beginning, and the entire degradation process is in a gentle state. From this point, the acidic environment will affect the rate at which BCN/CoN
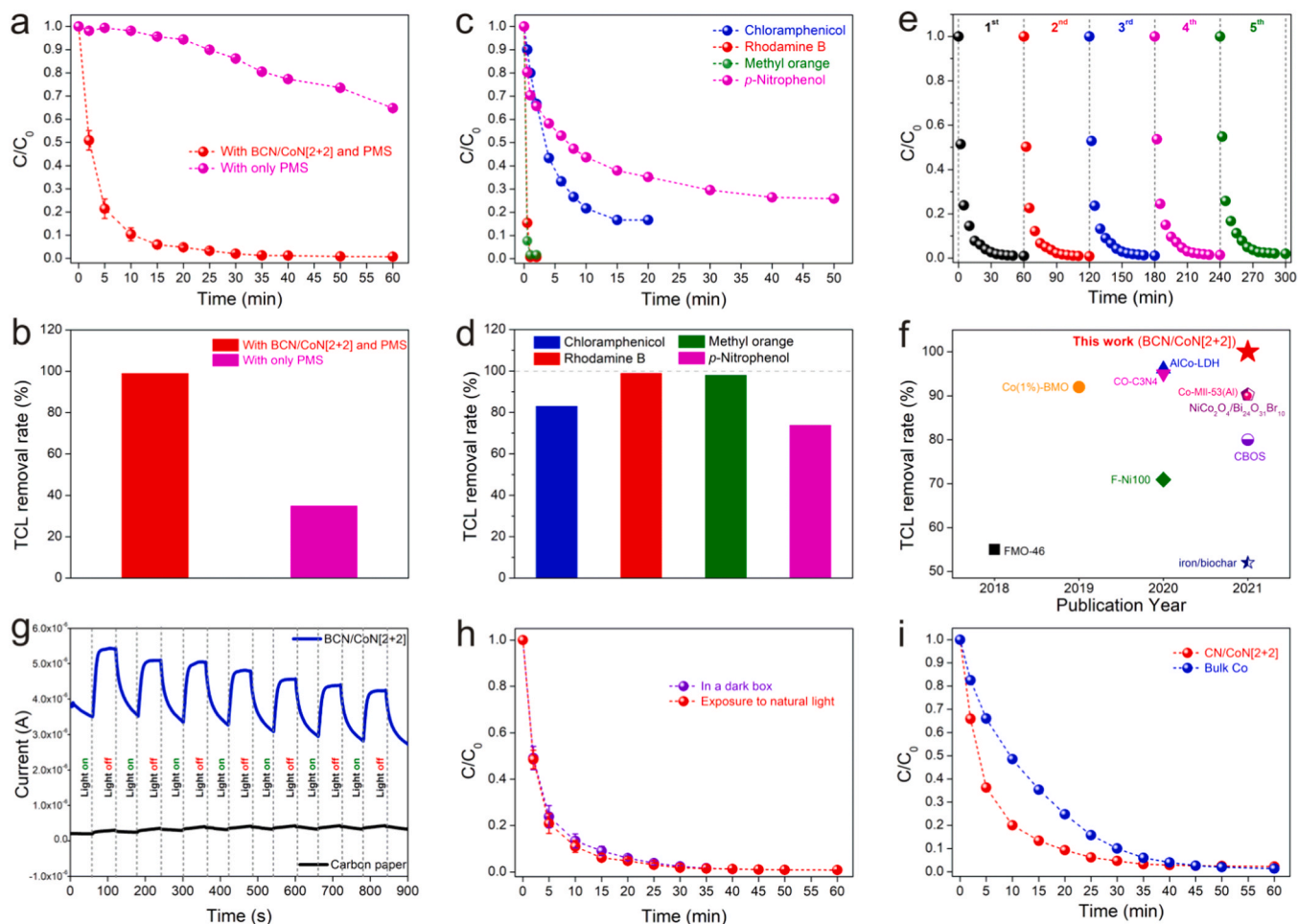
Fig. 4. a-b) The results of catalytic degradation TCL were obtained by using BCN/CoN[2 + 2], BCN/CoN[2 + 2]− 1 and BCN/CoN[2+2]−2 as catalysts, (TCL: 50 mg L⁻¹, Catalyst: 30 mg, PMS: 30 mg, pH = 7); **c-d)** Degradation results of different concentrations of TCL, (Catalyst: 30 mg BCN/CoN[2 +2], PMS: 30 mg, pH = 7); **e-f)** Degradation results of TCL in different pH value solutions, (TCL: 50 mg L⁻¹, Catalyst: 30 mg BCN/CoN[2 +2], PMS: 30 mg); **g)** Dark adsorption experiment without PMS and subsequent degradation TCL process when PMS is included; **h)** FT-IR spectrum (before the adsorption TCL, when the adsorption TCL is in equilibrium, after adding PMS and reacting for 30 min) of BCN/CoN[2 + 2].

[2 + 2] activates PMS. It can be considered that Protons (H⁺) in an acidic environment are plausible to bind to the active site, Co (Co-based materials are effective hydrogen evolution catalysts), thereby hindering the frequency of contact between PMS and Co. Even so, BCN/CoN[2+2] can still degrade about 80% of TCL in 60 min under acidic conditions.

Further, the role of various participants in the degradation process of TCL was explored. It can be seen that without PMS, BCN/CoN[2 + 2] has a certain adsorption capacity for TCL (Fig. 4g). When the adsorption/desorption equilibrium was reached and PMS is added, the change trend of TCL concentration is consistent with the situation without dark adsorption. Fig. 4c has shown that the concentration of low-concentration TCL at the initial stage of degradation tends to decay faster. Here, the TCL residue in the solution after dark adsorption only accounts for half of the initial concentration, but the decay rate of the TCL concentration after adding PMS is similar to that without dark adsorption. For this, we got the answer from the FT-IR spectrum signal (Fig. 4h) of BCN/CoN[2 + 2] (before the adsorption TCL, when the adsorption TCL is in equilibrium, after adding PMS and reacting for 30 min). Before adsorption TCL, the FT-IR signal of BCN/CoN[2 + 2] does not contain the signal of TCL. The TCL signal peak appeared after the dark adsorption TCL reached equilibrium, and the TCL signal peak disappeared after adding PMS and reaction for 30 min. That is to say, whether TCL is distributed in the solution or distributed on the catalyst dispersed in the solution, the total amount of TCL in the reaction system is not changed, and the active oxygen released by the PMS can

simultaneously degrade the TCL at different positions. Therefore, after adding the catalyst, TCL is adsorbed and degraded at the same time, and the adsorption effect has little effect on the degradation rate of TCL in the reaction system. The FT-IR spectroscopy combined with the absorbance change of the solution indicated that the TCL was finally completely removed, whether it was attached to the catalyst or dispersed in the solution phase. Keeping the conditions set for the degradation process unchanged, in the absence of BCN/CoN[2+2], the concentration of TCL will also decrease by approximately about 30% within 60 min (Fig. 5a-b). The presence of ultraviolet light in natural light can slowly excite PMS, and thus a decrease in the TCL concentration can be observed.

The general applicability of the catalyst to the degradation of organic pollutants and the stability of its own physical and chemical properties determine whether it can be widely used. Based on this, the ability of BCN/CoN[2 + 2] to degrade common organic pollutants via ROS was evaluated (Fig. 5c-d). BCN/CoN[2 + 2] can almost completely degraded RhB and MO within 1 min; it degraded approximately 80% of chloramphenicol (CAP) and 60% of p-nitrophenol in 15 min. This indicates that NCB/CoN[2 + 2] is universally capable of degrading organic pollutants via ROS, and the difference in degradation kinetics is controlled by the structure of the target pollutant alone. Compared with TCL, RhB and Mo, the reason why CAP is more difficult to degrade is that it contains Cl element, which is extremely electronegativity, which leads to the difficulty of breaking the C-Cl bond. Due to the cross-linked

Fig. 5. a-b) The change of TCL concentration under different conditions (with catalyst and PMS, or only catalyst, or only PMS, pH=7); **c-d**) Degradation results of chloramphenicol (10 mg L^{-1}), rhodamine B (50 mg L^{-1}), methyl orange (50 mg L^{-1}) and p-nitrophenol (50 mg L^{-1}), (Catalyst: 30 mg BCN/CoN[2 +2], PMS: 30 mg, pH=7); **e**) Repeated use of BCN/CoN[2+2] to degrade TCL, (TCL: 50 mg L^{-1}, PMS: 30 mg, pH=7); **f**) The performance comparison of catalysts reported in the literature and BCN/CoN[2 + 2] in degradation of TCL pollutants (reaction time: 30 min; references are listed in Table S1); **g**) The photocurrent response of BCN/CoN [2 + 2] in dark room and 350 W xenon lamp cold light (electrolyte: 0.5 M Na$_2$SO$_4$; applied potential: 0.5 V vs SCE); **h**) BCN/CoN[2 + 2] drives PMS to degrade TCL in dark environment or under natural light; **i**) The results of catalytic degradation TCL were obtained by using CN/CoN[2 + 2] or bulk Co in Carbon black (TCL: 50 mg L^{-1}, Catalyst: 30 mg, PMS: 30 mg, pH=7).
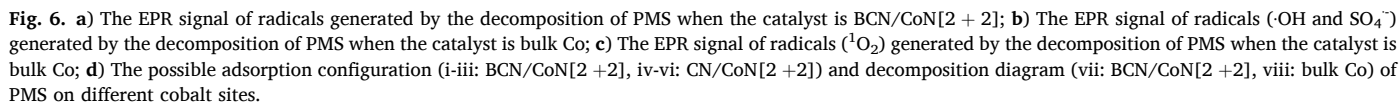
aromatic ring, TCL is more difficult to degrade than RhB and Mo, which have a looser π-electron atmosphere. Since the nitro group (Ar-NO$_2$) is a strong electron withdrawing group and will produce an electron withdrawing induction effect, the degradation of *p*-nitrophenol is more challenging. In addition, after repeated use of BCN/CoN[2 + 2] five times, its catalytic activity practically maintained its initial level (Fig. 5e), and the PXRD signal was similar to the initial state without generating the signal of nano-sized Co species (Fig. S5), which demonstrated its advantage in catalytic stability. The statistical results show that the performance of AOP driven by BCN/CoN[2 + 2] to degrade TCL is much better than the catalytic performance of recently reported catalysts (Fig. 5f, Table S1). To verify the effect of light on the degradation of TCL by BCN/CoN[2 + 2] via PMS, the photocurrent response of BCN/CoN[2 + 2] was measured. When using a 350 W xenon lamp cold light source (spot diameter of about 2 cm) to illuminate BCN/CoN[2 + 2], an obvious photocurrent signal was collected (Fig. 5g). Since the photocurrent signal of the carbon paper is so weak that it can be ignored, it is believed that the BCN/CoN[2 + 2] undergoes rapid charge transfer and separation at the internal interface under light driving [38,39]. However, when the reaction system is placed in a dark room, the reaction rate of BCN/CoN[2 + 2] to degrade TCL only slightly changes compared with that under natural light (Fig. 5h). Since the performance of BCN/CoN[2 + 2] driving PMS to degrade TCL in a dark room and under

natural light is similar, we first consider whether natural light can make BCN/CoN[2 + 2] generate photocurrent. The test results show that it is difficult to observe the generation of photocurrent signals in both natural light and darkroom switching back and forth (Fig. S6). In this case, operating the TCL degradation program in a dark room or in a natural light environment has little effect on the results of the study. Furtherre, the influence of the presence or absence of the B element in BCN/CoN [2 + 2] on driving PMS to degrade TCL was studied. In contrast, CN/CoN[2 + 2] as a catalyst for AOP showed a significantly lower degradation rate than BCN/CoN[2 + 2]; only 64% of the TCL could be eliminated within 5 min (Fig. 5i). When bulk Co was used as a catalyst, the TCL content at 5 min was attenuated by only 32%. This highlights the importance of the monoatomization of cobalt species and the introduction of B elements into the CN network to catalyze the degradation of TCL by AOP.

3.3. Possible mechanism of singlet oxygen generation

Determining the types of ROS in AOP is important for clarifying the structure of the catalyst and elucidating the catalytic mechanism. The types of radicals (or ROS) generated by BCN/CoN[2 + 2] and bulk Co to activate PMS were determined using EPR spectra. Obviously, under the stimulation of BCN/CoN[2 + 2], PMS only converts to ^{1}O$_2$, and·OH and

Fig. 6. a) The EPR signal of radicals generated by the decomposition of PMS when the catalyst is BCN/CoN[2 + 2]; **b)** The EPR signal of radicals (·OH and SO$_4^{·-}$) generated by the decomposition of PMS when the catalyst is bulk Co; **c)** The EPR signal of radicals ($^1O_2$) generated by the decomposition of PMS when the catalyst is bulk Co; **d)** The possible adsorption configuration (i-iii: BCN/CoN[2 +2], iv-vi: CN/CoN[2 +2]) and decomposition diagram (vii: BCN/CoN[2 +2], viii: bulk Co) of PMS on different cobalt sites.

SO$_4^{·-}$ are almost undetectable, and the proportion of $^1O_2$ is 100% (Fig. 6a). When bulk Co was used as a catalyst, in addition to $^1O_2$, it also produced·OH and·SO$_4^-$ (Fig. 6**b–c**). Based on this, it is believed that the active site (Co) in BCN/CoN[2 + 2] is in a completely different physicochemical environment from Co in bulk Co. Previous reports suggested that if the four N coordinated with Co form a closed-form (N–C–C–N–C–C–C–N–C–C–N–C–C–C), CoN$_4$ will preferentially adsorb the O atom connected to S in the PMS. In contrast, if the four N coordinated with Co are divided into two groups (N–C–C–N and N–C–C–N), CoN[2 + 2] preferentially adsorbs the O connected to –OH in the PMS. Therefore, we presume that the coordination of Co and N in BCN/CoN [2 + 2] is similar to that of CoN[2 + 2]. This presumption is based on the fact that the unpyrolyzed Co^{2+} forms a complex with 1,10-phenanthroline, and 1,10-phenanthroline is isolated from each other. Therefore, the coordination mode between Co^{2+} and 1,10-phenanthroline is CoN[2 + 2 + 2] (Co^{2+} usually presents a 6-coordination form). At pyrolysis temperatures up to 1000 °C, owing to the graphitization of organic species, it is difficult for Co to continue chelating with N in a form with coordination number 6 (with strong strain effect), and the favorable form is to transform into a planar tetra-coordination configuration. With the introduction of *closo*-[B$_{12}$H$_{12}$]$^{2-}$, the B atom in the high-temperature pyrolysis process assumes the task of bridging the edge C between two 1,10-phenanthroline. In our previous work, the BCN heterojunction formed the most stable structure in the form of C$_4$B$_2$N$_2$, in which B and N were cross-linked (Fig. S7) [40]. Combining the coordination configuration of 1,10-phenanthroline and Co^{2+}, the structure of CoN[2 + 2] was introduced into the C$_4$B$_2$N$_2$ model (Fig. 6**d(i)**).

Among them, the edges C connected to N in the two 1,10-phenanthro-line-like structures are bridged by the B atom. For comparison, after replacing all B in BCN/CoN[2 + 2] with C atoms, a CN/CoN[2 + 2] structure without B was obtained (Fig. 6**d(iv)**).

We observed that the adsorption energy of O1 and O2 in PMS on the Co site in BCN/CoN[2 + 2] is − 0.43 eV (the binding energy is 0.76 eV), and − 0.41 eV (the binding energy is 0.74 eV), respectively (Fig. 6**d(ii)– (iii)**). The adsorption energy of O1 on Co site in CN/CoN[2 + 2] is 0.06 eV (0.58 eV), and the adsorption energy of O2 on Co site is 0.02 eV (0.56 eV) (Fig. 6**d(v)-(vi)**). It can be seen that the configuration formed by the bonding of Co in BCN/CoN[2 + 2] with O1 of PMS is the most stable configuration. Compared with CN/CoN[2 + 2], the adsorption of PMS on BCN/CoN[2 + 2] is easier to attain. The electronegativity of electron-deficient B is only 2.04; however, the electronegativity of C and electron-rich N are 2.55 and 2.85, respectively [41]. C atom connected to N atom will be negatively charged, while C atom connected to B atom will be more positively charged. The electrical properties of C are transferred to the Co site, and the electron-deficient Co is likely to be attacked by O in PMS. In AOP where PMS participates, metal sites are usually the active centers. Since Co in BCN/CoN[2 + 2] exists in the form of a single atom, only one O can be allowed to contact the Co site in PMS. When O1 and BCN/CoN[2 + 2] formed the most stable adsorption configuration, the O1–S bond and O1–O3 bond are in an activated state (Fig. 6**d(vii)**). After O1 is connected to Co, O3 easily attacks the S atom connected to O1, thereby breaking the O1–S bond and O1–O3 bond and forming a new O3–S bond. The active O1 remaining at the Co site on BCN/CoN[2 + 2] eventually forms $^1O_2$. Because Co atom in bulk Co is
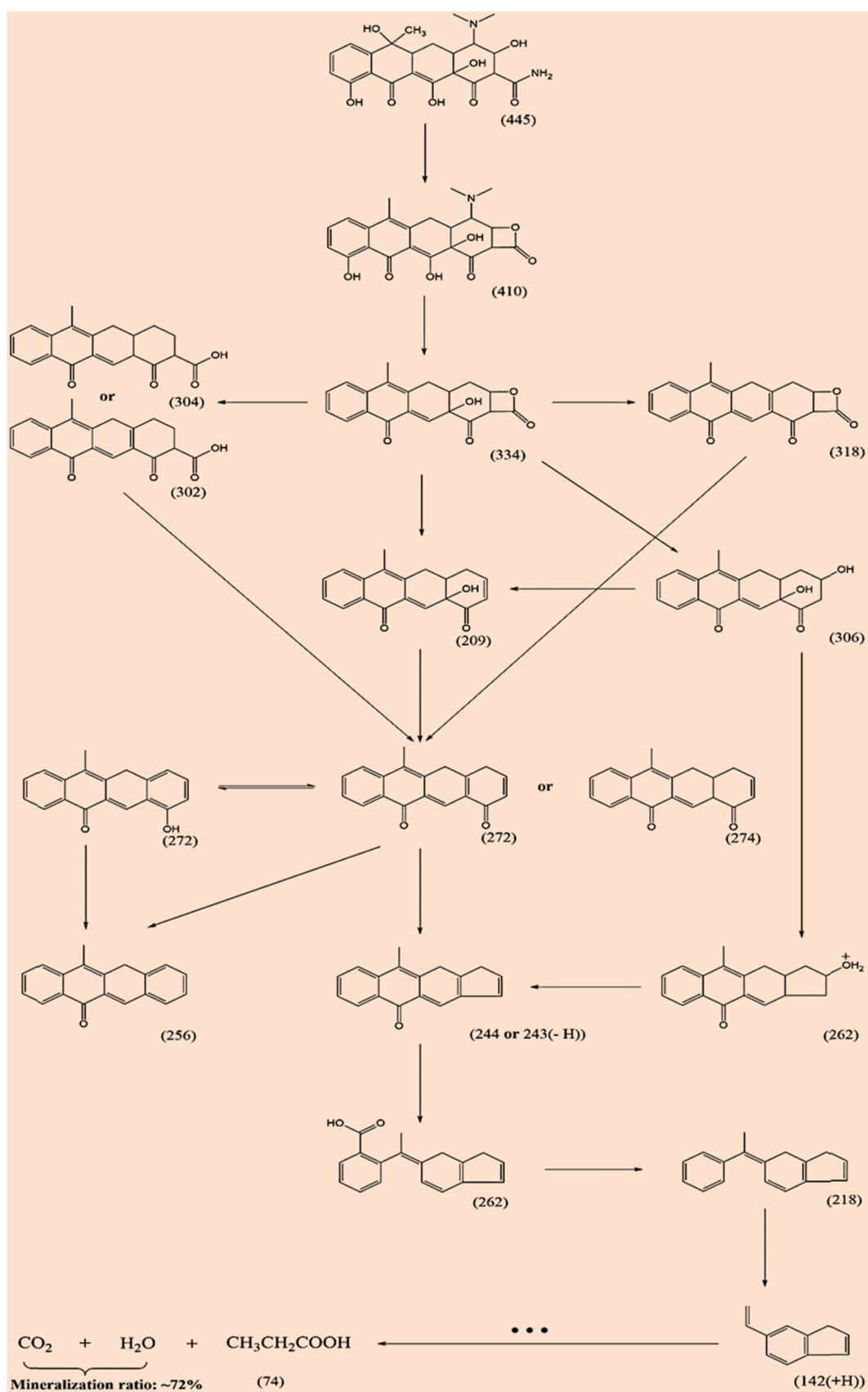
Fig. 7. The possible pathway for PMS to promote TCL degradation driven by BCN/CoN[2 + 2].

closely connected each other, O1 in PMS and O connected to S may be captured by the Co site. When O1 and O2 are adsorbed on the Co site, –OH is in a swinging state, so the O1–O3 bond is in an unstable state (Fig. 6**d(viii))**. After the O1-O3 bond is broken, ·OH and·SO$_4^-$ are formed. Of course, there will be cases where only O1 in PMS is connected to Co, so PMS can also be converted to $^1O_2$. The time required to adsorb only O1 is shorter than that required for the simultaneous adsorption of O1 and O2; therefore, ROS can be produced faster and act on organic pollutants, which is consistent with the experiment illustrated in Fig. 5**f**.

3.4. TCL degradation pathway

To determine the degradation path of TCL under the action of ROS, the intermediate species produced in the AOP process were monitored by liquid chromatography-mass spectrometry (LC-MS) (Figs. S8-S14). The non-ionic form of $^1O_2$ is different from SO$_4^-$ or·OH, and it does not cause a large increase in the specific charge (m/z) of the original TCL. TCL (M = 445) predominantly degrades according to the path shown in Fig. 7 until it is mineralized into CO_2 and H_2O (mineralization ratio is approximately 72%). Among them, intermediate substances were species with m/z values of 410, 334, 318, 304 (302), 306, 209, 272, 262, 244, 218, 142, and 74. We found that the degradation pathway of TCL by BCN/CON[2 + 2] is completely different from that of other catalysts that produce a variety of ROS in AOP [42]. This can be attributed to the substantiality that AOP driven by BCN/CoN[2 + 2] only produces a single type of ROS; therefore, the path of degradation of TCL is different from that of other catalysts. This is the first study where $^1O_2$ was used as ROS to degrade TCL, and the elucidated degradation mechanism provides a base for the degradation of pollutants in the future.

4. Conclusion

With 1,10-phenanthroline with N coordination sites as the rigid framework, large-size *closo*-[B$_{12}$H$_{12}$]$^{2-}$ as the counter anion and structural confinement component, successfully anchored Co^{2+} in isolation from each other to the metal boron clusters organic polymers. Following annealing, Co was uniformly distributed in the BCN matrix in the form of single atoms. AOP driven by BCN/CoN[2 + 2] can efficiently degrade TCL pollutants, and it only takes 5 min and 30 min to degrade TCL close to 80% and 100%, respectively. AOP with BCN/ CON [2 + 2] participation not only degrades TCL in a wide pH range, but also has the ability to efficiently degrade other common pollutants, even for inert chloramphenicol, showing a degradation ratio of up to 80%. In addition, BCN/CoN[2 + 2] also showed excellent stability in the AOP system, and its catalytic activity did not decay even if it was used repeatedly five times. EPR shows that BCN/CoN[2 + 2] drives the complete conversion of PMS into singlet oxygen, and density functional theory calculations demonstrate that the grounds for the conversion of PMS to singlet oxygen is owing to the isolated state of the active site Co. This achievement not only provides an excellent catalyst for the degradation of TCL, but also provides an important reference for the degradation mechanism of AOP involving different ROS.

CRediT authorship contribution statement

Xue Zhao: Conceptualization, Validation, Investigation, Resources, Data Curation, Writing - original draft, Visualization. **Xue Li**: Conceptualization, Validation, Resources, Data curation, Writing - original draft, Visualization. **Zhu Zhu**: Resources, Investigation. **Wanbiao Hu**: Writing - review & editing. **Haibo Zhang**: Resources, Writing - review & editing. **Jian Xu**: Writing - review & editing. **Xun Hu**: Writing - review & editing. **Yingtang Zhou**: Validation, Investigation; Software; Visualization; Writing - review & editing. **Ming Xu**: Resources; Investigation; Software; Visualization; Writing - review & editing. **Hucai Zhang**: Writing - review & editing. **Guangzhi Hu**: Conceptualization, Resources, Writing - review & editing, Supervision, Project administration,

Funding acquisition.

Declaration of Competing Interest

The authors declare that they have no known competing financial interests or personal relationships that could have appeared to influence the work reported in this paper.

Appendix A. Supporting information

Supplementary data associated with this article can be found in the online version at doi:10.1016/j.apcatb.2021.120759.

References

[1] F. Chen, Q. Yang, Y. Wang, F. Yao, Y. Ma, X. Huang, X. Li, D. Wang, G. Zeng, H. Yu, Efficient construction of bismuth vanadate-based Z-scheme photocatalyst for simultaneous Cr(VI) reduction and ciprofloxacin oxidation under visible light: kinetics, degradation pathways and mechanism, Chem. Eng. J. 348 (2018) 157–170.

[2] X. Zhao, D. Wang, C. Xiang, F. Zhang, L. Liu, X. Zhou, H. Zhang, Facile synthesis of boron organic polymers for efficient removal and separation of methylene blue, Rhodamine B, and Rhodamine 6G, ACS Sustain. Chem. Eng. 6 (2018) 16777–16787.

[3] X. Zhao, F. Zhang, H. Chen, R. Sheng, G.V. Baryshnikov, H. Ågren, X. Zhou, H. Zhang, Hydrophobic boron organic polymers: ultra-high capacity of enrichment and storage for chloroform, Chem. Eng. J. 385 (2020), 123827.

[4] X. Li, X. Zhao, X. Li, X. Jia, F. Chang, H. Zhang, G. Hu, Rapid simultaneous removal of cationic dyes and Cr(vi) by boron cluster polyaniline with a target site, Chem. Commun. (Camb.) 57 (2021) 7569–7572.

[5] X. Ma, K. Chen, B. Niu, Y. Li, L. Wang, J. Huang, H. She, Q. Wang, Preparation of BiOCl$_{0.9}$I$_{0.1}$/β-Bi$_2$O$_3$ composite for degradation of tetracycline hydrochloride under simulated sunlight, Chin. J. Catal. 41 (2020) 1535–1543.

[6] Z. Cao, Y. Jia, Q. Wang, H. Cheng, High-efficiency photo-Fenton Fe/g-C$_3$N$_4$/ kaolinite catalyst for tetracycline hydrochloride degradation, Appl. Clay Sci. 212 (2021), 106213.

[7] C. Gong, F. Chen, Q. Yang, K. Luo, F. Yao, S. Wang, X. Wang, J. Wu, X. Li, D. Wang, G. Zeng, Heterogeneous activation of peroxymonosulfate by Fe-Co layered doubled hydroxide for efficient catalytic degradation of Rhoadmine B, Chem. Eng. J. 321 (2017) 222–232.

[8] K.-Y.A. Lin, Z.-Y. Zhang, Degradation of Bisphenol A using peroxymonosulfate activated by one-step prepared sulfur-doped carbon nitride as a metal-free heterogeneous catalyst, Chem. Eng. J. 313 (2017) 1320–1327.

[9] L. Wang, X. Ma, G. Huang, R. Lian, J. Huang, H. She, Q. Wang, Construction of ternary CuO/CuFe2O4/g-C3N4 composite and its enhanced photocatalytic degradation of tetracycline hydrochloride with persulfate under simulated sunlight, J. Environ. Sci. 112 (2022) 59–70.

[10] X. Chen, X. Qiao, D. Wang, J. Lin, J. Chen, Kinetics of oxidative decolorization and mineralization of Acid Orange 7 by dark and photoassisted Co^{2+}-catalyzed peroxymonosulfate system, Chemosphere 67 (2007) 802–808.

[11] Q. Yang, Y. Ma, F. Chen, F. Yao, J. Sun, S. Wang, K. Yi, L. Hou, X. Li, D. Wang, Recent advances in photo-activated sulfate radical-advanced oxidation process (SR-AOP) for refractory organic pollutants removal in water, Chem. Eng. J. 378 (2019), 122149.

[12] S. Wacławek, H.V. Lutze, K. Grübel, V.V.T. Padil, M. Černík, D.D. Dionysiou, Chemistry of persulfates in water and wastewater treatment: a review, Chem. Eng. J. 330 (2017) 44–62.

[13] R.L. Johnson, P.G. Tratnyek, R.O.B. Johnson, Persulfate persistence under thermal activation conditions, Environ. Sci. Technol. 42 (2008) 9350–9356.

[14] A. Ghauch, G. Ayoub, S. Naim, Degradation of sulfamethoxazole by persulfate assisted micrometric Fe0 in aqueous solution, Chem. Eng. J. 228 (2013) 1168–1181.

[15] H. Hori, Y. Nagano, M. Murayama, K. Koike, S. Kutsuna, Efficient decomposition of perfluoroether carboxylic acids in water with a combination of persulfate oxidant and ultrasonic irradiation, J. Fluor. Chem. 141 (2012) 5–10.

[16] A. Ghauch, A. Baalbaki, M. Amasha, R. El Asmar, O. Tantawi, Contribution of persulfate in UV-254nm activated systems for complete degradation of chloramphenicol antibiotic in water, Chem. Eng. J. 317 (2017) 1012–1025.

[17] M. Amasha, A. Baalbaki, S. Al Hakim, R. El Asmar, A. Ghauch, Degradation of a toxic molecule o-Toluidine in industrial effluents using UV254/PS system, J. Adv. Oxid. Technol. 21 (2018) 261–273.

[18] W. Zhang, Y. He, C. Li, X. Hu, S. Yang, X. You, W. Liang, Persulfate activation using Co/AC particle electrodes and synergistic effects on humic acid degradation, Appl. Catal. B: Environ. 285 (2021), 119848.

[19] H. Song, R. Du, Y. Wang, D. Zu, R. Zhou, Y. Cai, F. Wang, Z. Li, Y. Shen, C. Li, Anchoring single atom cobalt on two-dimensional MXene for activation of peroxymonosulfate, Appl. Catal. B: Environ. 286 (2021), 119898.

[20] X. Su, X.-F. Yang, Y. Huang, B. Liu, T. Zhang, Single-atom catalysis toward efficient CO_2 conversion to CO and formate products, Acc. Chem. Res. 52 (2019) 656–664.

[21] Z. Xu, Y. Wu, Q. Ji, T. Li, C. Xu, C. Qi, H. He, S. Yang, S. Li, S. Yan, C. Sun, L. Zhang, Z. Zou, Understanding spatial effects of tetrahedral and octahedral cobalt cations on peroxymonosulfate activation for efficient pollution degradation, Appl. Catal. B: Environ. 291 (2021), 120072.

[22] L. Liu, A. Corma, Metal catalysts for heterogeneous catalysis: from single atoms to nanoclusters and nanoparticles, Chem. Rev. 118 (2018) 4981–5079.

[23] P. Hu, M. Long, Cobalt-catalyzed sulfate radical-based advanced oxidation: a review on heterogeneous catalysts and applications, Appl. Catal., B 181 (2016) 103–117.

[24] B.C. Hodges, E.L. Cates, J.-H. Kim, Challenges and prospects of advanced oxidation water treatment processes using catalytic nanomaterials, Nat. Nanotechnol. 13 (2018) 642–650.

[25] J. Liang, Y. Jiao, M. Jaroniec, S.Z. Qiao, Sulfur and nitrogen dual-doped mesoporous graphene electrocatalyst for oxygen reduction with synergistically enhanced performance, Angew. Chem. Int. Ed. 51 (2012) 11496–11500.

[26] H. Xu, N. Jiang, D. Wang, L. Wang, Y. Song, Z. Chen, J. Ma, T. Zhang, Improving PMS oxidation of organic pollutants by single cobalt atom catalyst through hybrid radical and non-radical pathways, Appl. Catal. B: Environ. 263 (2020), 118350.

[27] J. Yang, D. Zeng, J. Li, L. Dong, W.-J. Ong, Y. He, A highly efficient Fenton-like catalyst based on isolated diatomic Fe-Co anchored on N-doped porous carbon, Chem. Eng. J. 404 (2021), 126376.

[28] M. Chen, N. Wang, L. Zhu, Single-atom dispersed Co-N-C: A novel adsorption-catalysis bifunctional material for rapid removing bisphenol A, Catal. Today 348 (2020) 187–193.

[29] Y. Gao, Z. Chen, Y. Zhu, T. Li, C. Hu, New Insights into the generation of singlet oxygen in the metal-free peroxymonosulfate activation process: important role of electron-deficient carbon atoms, Environ. Sci. Technol. 54 (2020) 1232–1241.

[30] X. Mi, P. Wang, S. Xu, L. Su, H. Zhong, H. Wang, Y. Li, S. Zhan, Almost 100% peroxymonosulfate conversion to singlet oxygen on single-atom $CoN2+2$ sites, Angew. Chem. Int. Ed. 60 (2021) 4588–4593.

[31] V. Geis, K. Guttsche, C. Knapp, H. Scherer, R. Uzun, Synthesis and characterization of synthetically useful salts of the weakly-coordinating dianion [B12Cl12]2-, Dalton Trans. (2009) 2687–2694.

[32] X. Zhao, X. Li, Z. Bi, Y. Wang, H. Zhang, X. Zhou, Q. Wang, Y. Zhou, H. Wang, G. Hu, Boron modulating electronic structure of FeN4C to initiate high-efficiency oxygen reduction reaction and high-performance zinc-air battery, J. Energy Chem. (2021), https://doi.org/10.1016/j.jechem.2021.1008.1251.

[33] X. Zhao, H. Chen, H. Li, B. Hu, V.K. Artem, V.B. Glib, Å. Hans, W. Hu, G. Hu, X. Zhou, H. Zhang, Persistent radical-pairs trigger nano-gold to high-efficiently and high-selectively drive the value-added conversion of nitroaromatics, Chem. Catal. 1 (2021) 1–15.

[34] X. Zhao, Z. Yang, H. Chen, Z. Wang, X. Zhou, H. Zhang, Progress in three-dimensional aromatic-like closo-dodecaborate, Coord. Chem. Rev. 444 (2021), 214042.

[35] H. Duan, J.-C. Liu, M. Xu, Y. Zhao, X.-L. Ma, J. Dong, X. Zheng, J. Zheng, C.S. Allen, M. Danaie, Y.-K. Peng, T. Issariyakul, D. Chen, A.I. Kirkland, J.-C. Buffet, J. Li, S.C. E. Tsang, D. O'Hare, Molecular nitrogen promotes catalytic hydrodeoxygenation, Nat. Catal. 2 (2019) 1078–1087.

[36] M. Xu, S. Yao, D. Rao, Y. Niu, N. Liu, M. Peng, P. Zhai, Y. Man, L. Zheng, B. Wang, B. Zhang, D. Ma, M. Wei, Insights into interfacial synergistic catalysis over Ni@$TiO_{2−x}$ catalyst toward water–gas shift reaction, J. Am. Chem. Soc. 140 (2018) 11241–11251.

[37] H. Li, Y. Wen, M. Jiang, Y. Yao, H. Zhou, Z. Huang, J. Li, S. Jiao, Y. Kuang, S. Luo, Understanding of neighboring Fe-N4-C and Co-N4-C dual active centers for oxygen reduction reaction, Adv. Funct. Mater. 31 (2021), 2011289.

[38] H. Dong, Y. Zuo, N. Song, S. Hong, M. Xiao, D. Zhu, J. Sun, G. Chen, C. Li, Bimetallic synergetic regulating effect on electronic structure in cobalt/vanadium co-doped carbon nitride for boosting photocatalytic performance, Appl. Catal. B: Environ. 287 (2021), 119954.

[39] H. Dong, S. Hong, P. Zhang, S. Yu, Y. Wang, S. Yuan, H. Li, J. Sun, G. Chen, C. Li, Metal-free Z-scheme 2D/2D VdW heterojunction for high-efficiency and durable photocatalytic H_2 production, Chem. Eng. J. 395 (2020) 125150.

[40] X. Zhao, Z. Yang, A.V. Kuklin, G.V. Baryshnikov, H. Ågren, W. Liu, H. Zhang, X. Zhou, BCN-Encapsulated nano-nickel synergistically promotes ambient electrochemical dinitrogen reduction, ACS Appl. Mater. Interfaces 12 (2020) 31419–31430.

[41] X. Feng, Y. Bai, M. Liu, Y. Li, H. Yang, X. Wang, C. Wu, Untangling the respective effects of heteroatom-doped carbon materials in batteries, supercapacitors and the ORR to design high performance materials, Energy Environ. Sci. 14 (2021) 2036–2089.

[42] J. Cao, S. Sun, X. Li, Z. Yang, W. Xiong, Y. Wu, M. Jia, Y. Zhou, C. Zhou, Y. Zhang, Efficient charge transfer in aluminum-cobalt layered double hydroxide derived from Co-ZIF for enhanced catalytic degradation of tetracycline through peroxymonosulfate activation, Chem. Eng. J. 382 (2020), 122802.